Composites Part B 188 (2020) 107885

Contents lists available at ScienceDirect

Composites Part B

journal homepage: www.elsevier.com/locate/compositesb

Multiscale modelling of scaling effects in the impact response of plain woven composites

Z.W. Xu [a], Y.H. Chen [b], W.J. Cantwell [c], Z.W. Guan [a,d,*]

[a] Department of Civil Engineering, University of Liverpool, Liverpool, L69 3GH, UK
[b] Department of Engineering Science, University of Oxford, Oxford, OX1 3PJ, UK
[c] Department of Aerospace Engineering, Khalifa University, Abu Dhabi, United Arab Emirates
[d] School of Mechanical Engineering, Chengdu University, Shiling Town, Chengdu, PR China

ARTICLE INFO

Keywords:
Multiscale modelling
Scaling effects
Low-velocity impact
Plain woven composites

ABSTRACT

This paper presents a multiscale model developed to predict scaling effects in plain woven carbon fibre-reinforced polymer (CFRP) composites. The model contains a parameter-segmented unit cell (UC) developed to account for the contribution of the fabric architecture to the macroscopic response. The behaviour of constituent materials was considered by employing the models that have been established for characterising the nonlinearity and rate-dependence of the polymer matrix and the damage of the yarn material. A user subroutine was developed to numerically implement the parameterised UC and the material models for multiscale analyses. Based on the multiscale model, numerical examples were performed to investigate scaling effects in the impact response of a plain woven composite by simulating scaled panels subjected to projectile impact. It is shown that the proposed model is capable of predicting both scalable and non-scalable effects in this composite with reasonable success. The simulation results highlighted an evident variation of the load-displacement curves with scale size at the post-elastic stage, insensitivities of the primary failure modes and their appearance to scale size, as well as a clear trend of increased capability of energy absorption with scale size, which all agree well with those observed in experiments. The significance of this research is the development of a numerical tool capable of capturing the influence of microscopic features on macroscopic scaling effects in plain woven composites.

1. Introduction

Compared to traditional materials, fibre-reinforced polymer (FRP) composites offer many attractive characteristics including high specific strength and stiffness, improved impact resistance, increased design flexibility, superior stability and durability. These desirable features have naturally stimulated intensive applications of fibre reinforced composites in engineering products of many industry sectors, such as composite wings and airframe structures in the aerospace sector, fully integrated composite body-in-white in the automotive industry and composite blades in the wind energy industry. However, masked by the great success and widespread usage of the composites, there is an easily ignored concern originating from a common design practice of developing large composite structures or components based on small-scale models to save time and costs. However, composites may exhibit significant scaling effects, with their mechanical properties and response being dependent on geometry or scale size, e.g. increased strength with decreasing scale size. As a result, developing a composite structure without completely exploring scaling effects may result in a potentially invalid design in the first place and possibly catastrophic outcomes to the end-user.

Given the critical importance of understanding scaling effects, a good variety of studies have been conducted in the past decades to experimentally investigate the effects of geometry or scale size on the mechanical properties and response of different types of unidirectional (UD) composites subjected to different loading conditions. Initial research focused on investigating scaling effects in the quasi-static properties of unnotched composites [1–4] and composites with geometrical discontinuities such as notches and holes [5–7], highlighting that composites largely exhibit decreased strength values with increasing scale size. Research studies were also performed to quantify scaling effects in the dynamic response of FRP composites [8–10]. In those studies, the dependences of response parameters such as impact force, impact damage, area of delamination and energy absorption on

* Corresponding author. Department of Civil Engineering, University of Liverpool, Liverpool, L69 3GH, UK.
E-mail address: zguan@liv.ac.uk (Z.W. Guan).

https://doi.org/10.1016/j.compositesb.2020.107885
Received 22 October 2019; Received in revised form 13 February 2020; Accepted 13 February 2020
Available online 19 February 2020

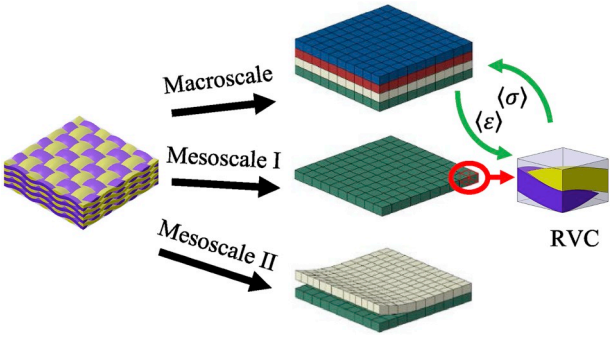

Fig. 1. Schematic of the proposed multiscale modelling strategy.

scale size were identified. Apart from typical FRP composites, experimental investigations were also conducted to study scaling effects in fibre-metal composites and honeycomb sandwich structures with composite skins [11–13]. The results of these studies indicate that the addition of non-FRP ingredients in composites generally reduces the dependency of the impact response of these composites on scale size. An examination of the publications outlined above reveals that most of the existing studies on scaling effects in composites focused on unidirectional composites, with little attention paid to textile composites, although they offer superior impact performance compared to their UD counterparts. Also, these studies were undertaken primarily based on experimental testing, limiting the possibility of implementing the gained knowledge of scaling effects into the design of composite structures at an early stage, by means of performing numerical analyses and simulations.

Numerous theories fulfilling various aspects of multiscale modelling have been reported in the literature. To account for the influence of the internal fabric architecture on the macroscopic behaviour, sophisticated micromechanical models have been developed by researchers including Ishikawa and Chou [14], Wentorf et al. [15], Lomov et al. [16], Whitcomb and Tang [17], Sun et al. [18], Li et al. [19], Lin et al. [20] and Green et al. [21], among many others. In terms of damage modelling of FRP composites, different kinds of criteria associated with failure modes have been proposed, featuring those formulated by Hashin [22], Puck and Schurmann [23], Pinho et al. [24] and others, as reviewed by Kaddoura et al. [25] on the World-Wide Failure Exercise (WWFE). Research studies have been performed to describe the nonlinearity and rate-dependence of FRP composites by means of adapting viscoplasticity theories. Notable models on this topic include those developed by Fish and Shek [26], Goldberg et al. [27] and Weeks and Sun [28].

In spite of numerous theories previously proposed for modelling textile composites, there is still a lack of predictive models that have been validated for numerical investigation of scaling effects in textile composites. The current work aims to fill such a gap by means of developing a predictive model for textile composites using a multiscale modelling approach, rather than taking a micromechanical approach. This is because scaling effects in textile composites are closely associated with the hierarchical nature of textile composites and differences in the microscopic features at different scale sizes. For example, in a set of scaled composite laminates with the actual numbers of plies in these laminates being 4, 8, 12 and 16, the normalised numbers of ply interfaces of these laminates are different and equal to 3/4, 7/8, 11/12 and 15/16, which may result in scaling effects in the resistance to interlaminar delamination. Another example is that some microscopic features of textile composite laminates (e.g. the width of fabric yarns) do not scale with macroscopic features such as the length and thickness of the laminates. Thus, it is of critical importance to employ a multiscale modelling strategy so that the contribution of microscopic features to macroscopic behaviour can be reasonably considered. However, instead

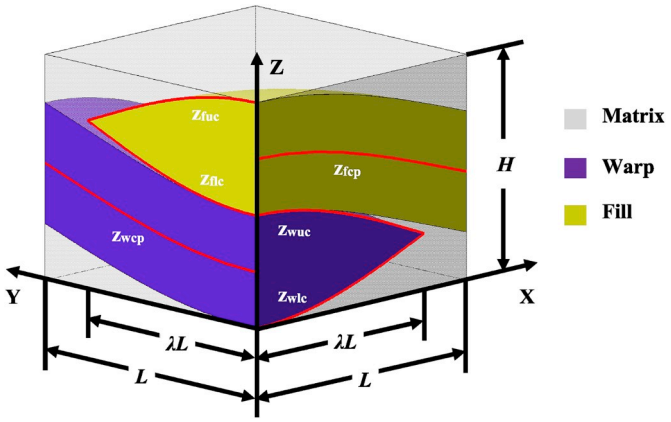

Fig. 2. Proposed unit cell of plain woven composites.

of developing novel theories for all aspects of the multiscale model, the present research specifically focuses on bridging and improving existing theories to form a multiscale approach that is capable of predicting scaling effects in the impact response of plain woven composites, with emphasis on modelling a parameterised unit cell (UC) and numerically investigating scaling effects in the load-displacement response, failure mechanisms and energy absorption.

2. Multiscale modelling

In the proposed multiscale modelling strategy, a plain woven composite laminate is modelled at three length scales, as shown in Fig. 1. At the macroscale, the laminate is treated as a multi-layer solid, with each layer representing a composite lamina or ply. In addition, each layer is discretised with elements, whose response is represented by homogenising a representative volume cell (RVC), where modelling at mesoscale I is conducted to analytically consider the internal architecture (i.e. cross-section and waviness of the yarns) and the behaviour of the individual constituents (e.g. the nonlinear, rate-dependent deformation of the polymer matrix and the development of anisotropic damage in the yarn material). In this way, the effects of both the microscopic features and the response of the individual constituents on the overall response (including scaling effects) can be captured. Further, the division of the laminate into a multi-layer solid allows for modelling interlaminar delamination at mesoscale II.

2.1. Modelling at mesoscale I

2.1.1. Parametrised unit cell modelling

To correlate the macroscopic behaviour of plain woven composites with the microscopic geometry and material behaviour of the individual constituents, a UC considering the internal architecture was defined, as shown in Fig. 2. Here, it should be noted that the proposed UC is only 1/16 of the full-size UC and was obtained by exploiting the translational, rotational and reflectional symmetries in the geometrical architecture of the composite [29]. The UC is comprised of a matrix phase and two yarns, with overall dimensions of $L \times L \times H$. Considering the microscopic features of the plain woven composite under investigation, as shown in Fig. 3, it was assumed that both the cross-sectional curves and waviness of the fibre yarns can be reasonably described using cosine or sine functions. In addition, a constant cross-section was assumed so that each yarn can be fully depicted using the cross-sectional and central path curves. Based on these assumptions and the geometrical relationships shown in Fig. 2, the internal architecture can be described as follows:

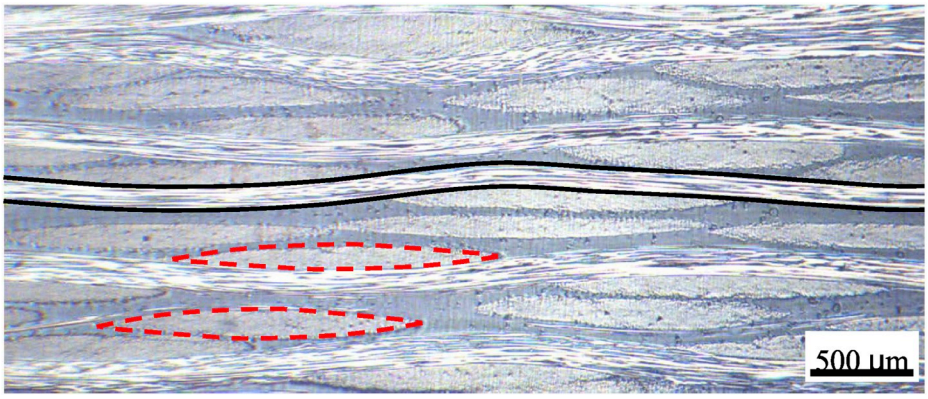

Fig. 3. Cross-section of the plain woven composite under investigation.

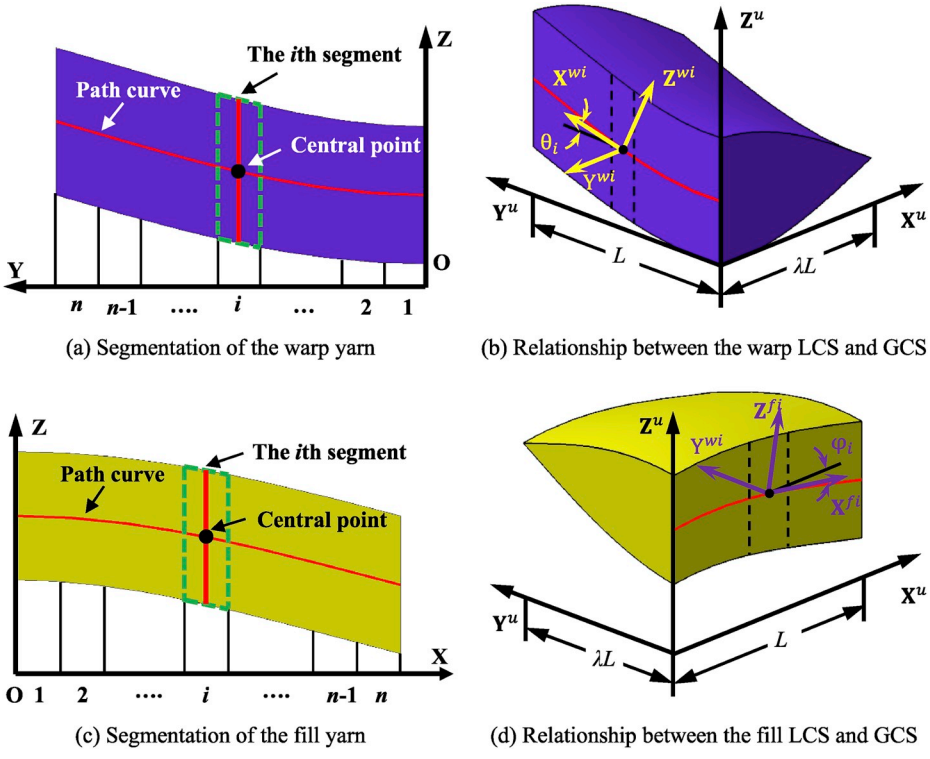

Fig. 4. Parameterised segmentation of the warp/fill yarns and relationships between the LCS and GCS.

$$\begin{Bmatrix} z_{\mathrm{wuc}} \\ z_{\mathrm{wlc}} \\ z_{\mathrm{wcp}} \\ \theta_{\mathrm{warp}} \end{Bmatrix} \begin{Bmatrix} \frac{H}{4}+\frac{H}{4}\cos\frac{\pi x}{2\lambda L} \\ \frac{H}{4}-\frac{H}{4}\cos\frac{\pi x}{2\lambda L} \\ \frac{H}{2}-\frac{H}{4}\cos\frac{\pi y}{2L} \\ \operatorname{atan}\left(\frac{\pi H}{8L}\sin\frac{\pi y}{2L}\right) \end{Bmatrix} \& \begin{Bmatrix} z_{\mathrm{fuc}} \\ z_{\mathrm{flc}} \\ z_{\mathrm{fcp}} \\ \phi_{\mathrm{fill}} \end{Bmatrix} = \begin{Bmatrix} \frac{3H}{4}+\frac{H}{4}\cos\frac{\pi y}{2\lambda L} \\ \frac{3H}{4}-\frac{H}{4}\cos\frac{\pi y}{2\lambda L} \\ \frac{H}{2}+\frac{H}{4}\cos\frac{\pi x}{2L} \\ \operatorname{atan}\left(\frac{\pi H}{8L}\sin\frac{\pi y}{2L}\right) \end{Bmatrix} \tag{1}$$

where λ is a dimensionless parameter introduced to control the width of the yarns; z_{wuc}, z_{wlc}, z_{wcp} and θ_{warp} represent the upper and lower cross-sectional curves, the central path curve and the waviness angle of the warp yarn; and z_{fuc}, z_{flc}, z_{fcp} and ϕ_{fill} represent the corresponding values for the fill yarn.

Although the use of cosine functions enables smooth descriptions of the warp and fill yarns, it creates extra complexity in a multiscale analysis in terms of computing the microscopic stresses of the UC. To address this problem, a parameter n was introduced to discretise the warp and fill yarns into n evenly distributed segments, as illustrated in Fig. 4(a) and (c). Based on such a parameterised discretisation, each segment of the yarns can be locally treated as a UD composite portion, with the volume fraction and orientation of the ith segment defined by:

$$\begin{Bmatrix} \theta_i \\ \phi_i \\ v^i_{\mathrm{warp}} \\ v^i_{\mathrm{fill}} \end{Bmatrix} = \begin{Bmatrix} \theta_{\mathrm{warp}}\left(y=\frac{2i-1}{2n}L\right) \\ -\phi_{\mathrm{fill}}\left(y=\frac{2i-1}{2n}L\right) \\ \frac{1}{nHL^2}\int_0^L\int_0^{\lambda L}(Z_{\mathrm{wuc}}-Z_{\mathrm{wlc}})dxdy \\ \frac{1}{nHL^2}\int_0^L\int_0^{\lambda L}(Z_{\mathrm{fuc}}-Z_{\mathrm{flc}})dxdy \end{Bmatrix} = \begin{Bmatrix} \operatorname{atan}\left(\frac{\pi H}{8L}\sin\frac{\pi(2i-1)}{4n}\right) \\ \operatorname{atan}\left(\frac{\pi H}{8L}\sin\frac{\pi(2i-1)}{4n}\right) \\ \frac{\lambda}{n\pi} \\ \frac{\lambda}{n\pi} \end{Bmatrix} \tag{2}$$

where θ_i (ϕ_i) denotes the ith segment of the warp (fill) yarn; and v^i_{warp} (v^i_{fill}) is the respective volume fraction of the segment. By segmenting the fibre yarns into smaller regions, a local coordinate system (LCS) is defined for each segment so that the constitutive modelling of the yarn material can be firstly addressed in the LCS (as shown in Fig. 4(b) and (d)) and transformed into the global coordinate system (GCS) of the UC, if needed, as follows:

$$\begin{Bmatrix} \boldsymbol{\sigma}^{ui} \\ \boldsymbol{\varepsilon}^{ui} \\ \mathbf{C}^{ui} \end{Bmatrix} = \begin{Bmatrix} \left(\mathbf{T}^{u|li}\right)^{\mathrm{T}}\boldsymbol{\sigma}^{li} \\ \left(\mathbf{T}^{u|li}\right)^{\mathrm{T}}\boldsymbol{\varepsilon}^{li} \\ \left(\mathbf{T}^{u|li}\right)^{\mathrm{T}}\mathbf{C}^{y}\mathbf{T}^{u|li} \end{Bmatrix} \tag{3}$$

where $\boldsymbol{\sigma}^{ui}$, $\boldsymbol{\varepsilon}^{ui}$ and $\mathbf{C}^{ui}$ refer to the stress vector, the tensorial strain vector and the elasticity matrix of the ith segment in the GCS; $\boldsymbol{\sigma}^{li}$, $\boldsymbol{\varepsilon}^{li}$ and $\mathbf{C}^{li}$ are the respective quantities in the LCS; and $\mathbf{T}^{u|li}$ represents the transformation matrix from the LCS to GCS and is defined in Eq. (4) for the warp yarn and Eq. (5) for the fill yarn, respectively:

$$\mathbf{T}^{u|li}_{\mathrm{warp}} = \begin{bmatrix} 0 & \cos^2\theta_i & \sin^2\theta_i & 0 & 0.5\sin(2\theta_i) & 0 \\ 1 & 0 & 0 & 0 & 0 & 0 \\ 0 & \sin^2\theta_i & \cos^2\theta_i & 0 & -0.5\sin(2\theta_i) & 0 \\ 0 & 0 & 0 & -\cos\theta_i & 0 & -\sin\theta_i \\ 0 & 0 & 0 & \sin\theta_i & 0 & -\cos\theta_i \\ 0 & -\sin(2\theta_i) & \sin(2\theta_i) & 0 & \cos(2\theta_i) & 0 \end{bmatrix} \tag{4}$$

$$\mathbf{T}^{u|li}_{\mathrm{fill}} = \begin{bmatrix} \cos^2\phi_i & 0 & \sin^2\phi_i & 0 & 0 & -0.5\sin(2\phi_i) \\ 0 & 1 & 0 & 0 & 0 & 0 \\ \sin^2\phi_i & 0 & \cos^2\phi_i & 0 & 0 & 0.5\sin(2\phi_i) \\ 0 & 0 & 0 & \cos\phi_i & -\sin\phi_i & 0 \\ 0 & 0 & 0 & \sin\phi_i & \cos\phi_i & 0 \\ \sin(2\phi_i) & 0 & -\sin(2\phi_i) & 0 & 0 & \cos(2\phi_i) \end{bmatrix} \tag{5}$$

2.1.2. Constitutive behaviour of polymer matrix

2.1.2.1. Nonlinearity and rate-dependence. Polymers are isotropic materials, with features such as nonlinearity and rate-dependence. Typically, they show viscoelastic behaviour at small strains and become nonlinear at large strains. Although the nonlinear, rate-dependent deformation of a polymer is primarily driven by the respective molecular mechanisms (e.g. the unwinding of molecular kinks) and may be modelled using a molecular approach, adopting a viscoplasticity-based model to describe the behaviour of a polymer is preferable from the point of view of simplicity. In this work, the nonlinearity and rate-dependence of polymer matrix are addressed using the viscoplasticity-based model developed by Goldberg et al. [27]. This model assumes that the total strain-rate, $\dot{\varepsilon}_{ij}$, is the sum of an elastic portion, $\dot{\varepsilon}^{\mathrm{E}}_{ij}$, and an inelastic portion, $\dot{\varepsilon}^{\mathrm{I}}_{ij}$, i.e. $\dot{\varepsilon}_{ij} = \dot{\varepsilon}^{\mathrm{E}}_{ij} + \dot{\varepsilon}^{\mathrm{I}}_{ij}$. In addition, the inelastic strain-rate is phenomenologically modelled as a function of several material parameters and state variables. The state variables in return evolve with respect to the inelastic strain-rate, resulting in a set of constitutive relations in a rate-dependent form or an increment form, as shown in the left or right side of Eq. (6):

$$\dot{\varepsilon}^{\mathrm{I}}_{ij} = D_0\exp\left(-\frac{1}{2}\left(\frac{Z}{\sigma_{\mathrm{eff}}}\right)^{2n_r}\right)\frac{S_{ij}}{\sqrt{J_2}} \qquad d\varepsilon^{\mathrm{I}}_{ij} = \left[D_0\exp\left(-\frac{1}{2}\left(\frac{Z}{\sigma_{\mathrm{eff}}}\right)^{2n_r}\right)\frac{S_{ij}}{\sqrt{J_2}}\right]dt$$

$$\begin{aligned} \sigma_{\mathrm{eff}} &= \sqrt{3J_2}+\alpha\sigma_{kk} & \sigma_{\mathrm{eff}} &= \sqrt{3J_2}+\alpha\sigma_{kk} \\ \dot{Z} &= q(Z_1-Z)\dot{e}^{\mathrm{I}}_{\mathrm{eff}} \quad \text{or} & dZ &= q(Z_1-Z)de^{\mathrm{I}}_{\mathrm{eff}} \\ \dot{\alpha} &= q(\alpha_1-\alpha)\dot{e}^{\mathrm{I}}_{\mathrm{eff}} & d\alpha &= q(\alpha_1-\alpha)de^{\mathrm{I}}_{\mathrm{eff}} \\ \dot{e}^{\mathrm{I}}_{\mathrm{eff}} &= \sqrt{\frac{2}{3}\dot{e}^{\mathrm{I}}_{ij}\dot{e}^{\mathrm{I}}_{ij}} & de^{\mathrm{I}}_{\mathrm{eff}} &= \sqrt{\frac{2}{3}de^{\mathrm{I}}_{ij}de^{\mathrm{I}}_{ij}} \end{aligned} \tag{6}$$

where D_0 is a constant denoting the maximum inelastic strain-rate; n_{r} refers to a material parameter used to describe the dependence of inelastic deformation on the strain-rate; σ_{eff} denotes the effective stress, which is employed to account for the effect of hydrostatic stresses on the rate-dependence; Z is the internal stress variable used to model the resistance to molecular flow; and J_2 represents the second invariant of the deviatoric stress, S_{ij}. In the above equation set, the effective stress evolves as a function of the mean stress, σ_{kk}, and a scaling factor, α. Also, both the internal stress and the mean stress scaling factor, whose initial (maximum) values are denoted by Z_0 (Z_1) and α_0 (α_1), are defined in the same form, evolving with the initial hardening rate, q, and the effective deviatoric inelastic strain-rate, $\dot{e}^{\mathrm{I}}_{\mathrm{eff}}$.

The constitutive model described above generates a differential

equation for each component of the state variables without a closed solution. To numerically solve the equations within the framework of a transient finite element solver, e.g. ABAQUS/Explicit, the standard fourth-order Runge-Kutta (RK) algorithm was applied to the incremental form of the constitutive equations to calculate the state variables at the current increment, $n+1$, based on their values at the previous increment, n, as follows:

$$\begin{aligned}
\varepsilon_{ij}^{\mathrm{I}(n+1)} &= \varepsilon_{ij}^{\mathrm{I}(n)} + \frac{1}{6}d\varepsilon_{ij}^{\mathrm{I}\langle 1\rangle} + \frac{1}{3}d\varepsilon_{ij}^{\mathrm{I}\langle 2\rangle} + \frac{1}{3}d\varepsilon_{ij}^{\mathrm{I}\langle 3\rangle} + \frac{1}{6}d\varepsilon_{ij}^{\mathrm{I}\langle 4\rangle} \\
Z^{(n+1)} &= Z^{(n)} + \frac{1}{6}dZ^{\langle 1\rangle} + \frac{1}{3}dZ^{\langle 2\rangle} + \frac{1}{3}dZ^{\langle 3\rangle} + \frac{1}{6}dZ^{\langle 4\rangle} \\
\alpha^{(n+1)} &= \alpha^{(n)} + \frac{1}{6}d\alpha^{\langle 1\rangle} + \frac{1}{3}d\alpha^{\langle 2\rangle} + \frac{1}{3}d\alpha^{\langle 3\rangle} + \frac{1}{6}d\alpha^{\langle 4\rangle} \\
\sigma_{ij}^{(n+1)} &= c_{ijkl}\left(\varepsilon_{kl}^{(n+1)} - \varepsilon_{kl}^{\mathrm{I}(n+1)}\right)
\end{aligned} \tag{7}$$

where $d\varepsilon_{ij}^{\mathrm{I}\langle i\rangle}$, $dZ^{\langle i\rangle}$ and $d\alpha^{\langle i\rangle}$ are the increments of the corresponding variables and computed at the ith step of the RK algorithm; and c_{ijkl} represents the elasticity tensor, with each component being a function of the elastic modulus, E_{m}, and Poisson's ratio, ν_{m}.

2.1.2.2. Damage initiation and evolution. Although the Goldberg model describes the nonlinear and rate-dependent deformation response of a polymer, it does not identify the point at which damage initiates and how damage propagates after damage initiation. Assuming that the stress-strain curve of a polymer matrix beyond the yield point is typically insensitive to stress, the following strain-based criterion is employed to determine the onset of damage:

$$f_{\mathrm{m}} = \left|\frac{\varepsilon_{\mathrm{eff}}}{\varepsilon_{\mathrm{mf}}}\right| = 1 \tag{8}$$

where f_{m} represents the failure function; $\varepsilon_{\mathrm{mf}}$ is a material parameter denoting the ultimate failure strain; and $\varepsilon_{\mathrm{eff}}$ the effective total strain. Here, the ultimate failure strain is assumed to vary with strain-rate as a result of the rate-dependence of the polymer matrix. To model such an effect, the logarithmic approach originally proposed by Weeks and Sun [28] is adapted to scale the ultimate failure strain, as follows:

$$\varepsilon_{\mathrm{mf}} = \begin{cases} \varepsilon_{\mathrm{m0}}\left(1 \pm C_{m\varepsilon}\ln\dfrac{|\dot{\varepsilon}|}{\dot{\varepsilon}_0}\right) & |\dot{\varepsilon}| \geq \dot{\varepsilon}_0 \\ \varepsilon_{\mathrm{m0}} & |\dot{\varepsilon}| < \dot{\varepsilon}_0 \end{cases} \tag{9}$$

where $\dot{\varepsilon}$ denotes the effective strain-rate; $\dot{\varepsilon}_0$ is reference strain-rate; $\varepsilon_{\mathrm{m0}}$ represents the ultimate failure strain measured at the reference strain-rate; and $C_{m\varepsilon}$ is a material constant reflecting the dependence of the ultimate failure strain on strain-rate. Here, it is worth noting that the positive sign should be used if the ultimate failure strain increases with strain-rate. If not, a negative sign is employed.

The polymer matrix under investigation is a highly toughened epoxy [30]. However, the polymer matrix is assumed to have a similar damage behaviour to the yarn material in the transverse direction. Thus, the Weibull distribution based formulation developed by Chen and Aliabadi [31] was simplified into a uniaxial form to describe the evolution of damage in the polymer matrix as follows:

$$\omega_{\mathrm{m}} = \begin{cases} 1 - \exp\left[-\dfrac{1}{e}\left(\left(\left|\dfrac{\varepsilon_{\mathrm{eff}}}{\varepsilon_{\mathrm{mf}}}\right|\right)^{\beta_{\mathrm{m}}} - 1\right)\right] & \left|\dfrac{\varepsilon_{\mathrm{eff}}}{\varepsilon_{\mathrm{mf}}}\right| > 1 \\ 0 & \left|\dfrac{\varepsilon_{\mathrm{eff}}}{\varepsilon_{\mathrm{mf}}}\right| \leq 1 \end{cases} \tag{10}$$

where ω_{m} represents the damage in the polymer matrix; letter "e" is the base of the natural logarithm; and β_{m} is a material parameter describing the rate of damage evolution, a value that can be tuned after performing a regression analysis on a set of uniaxial tensile tests. Based on Eq. (10), the degradation of stiffness is represented by multiplying the elasticity matrix by a factor of $(1-\omega_{\mathrm{m}})$. Thus, the stress after damage initiation is updated as follows, where ε_{kl}^{Id} denotes the maximum inelastic strain prior to damage:

$$\sigma_{ij}^{(n+1)} = (1-\omega_{\mathrm{m}})c_{ijkl}\left(\varepsilon_{kl}^{(n+1)} - \varepsilon_{kl}^{Id}\right) \tag{11}$$

2.1.3. Constitutive behaviour of yarn material

2.1.3.1. Anisotropic damage initiation. Since the fibre yarns in the plain woven composites have been analytically modelled with their orientations defined in Eq. (2), they are essentially UD composites in the LCS. Thus, the yarn material was similarly treated as a transversely-isotropic material exhibiting linear elastic behaviour up to damage initiation, followed by anisotropic damage evolution. In this work, the onset of damage of the yarn material was addressed by generalising the Hashin failure criteria [22] by means of introducing two additional failure modes associated with the thickness direction [31]. Given the isotropic nature of the yarn material in the transverse directions, the two additional failure modes were defined similarly to those associated with the in-plane transverse direction. Therefore, six damage modes are defined to identify the initiation of damage of the yarn material:

$$\begin{aligned}
f_{1\mathrm{fT}} &= \left(\frac{\langle\sigma_{11}\rangle}{X_{\mathrm{T}}}\right)^2 + \frac{\tau_{12}^2}{S_{12}^2} + \frac{\tau_{31}^2}{S_{31}^2} = 1 \\
f_{1\mathrm{fC}} &= \left(\frac{-\sigma_{11} - \langle -\frac{\sigma_{22}+\sigma_{33}}{2}\rangle}{X_{\mathrm{C}}}\right)^2 = 1 \\
f_{2\mathrm{mT}} &= \left(\frac{\langle\sigma_{22}\rangle}{Y_{\mathrm{T}}}\right)^2 + \frac{\tau_{12}^2}{S_{12}^2} + \frac{\tau_{23}^2}{S_{23}^2} = 1 \\
f_{2\mathrm{mC}} &= \left(\frac{\langle-\sigma_{22}\rangle}{2S_{23}}\right)^2 + \left[\left(\frac{Y_{\mathrm{C}}}{2S_{23}}\right)^2 - 1\right]\frac{\sigma_{22}}{Y_{\mathrm{C}}} + \frac{\tau_{12}^2}{S_{12}^2} = 1 \\
f_{3\mathrm{mT}} &= \left(\frac{\langle\sigma_{33}\rangle}{Z_{\mathrm{T}}}\right)^2 + \frac{\tau_{23}^2}{S_{23}^2} + \frac{\tau_{31}^2}{S_{31}^2} = 1 \\
f_{3\mathrm{mC}} &= \left(\frac{\langle-\sigma_{33}\rangle}{2S_{23}}\right)^2 + \left[\left(\frac{Z_{\mathrm{C}}}{2S_{23}}\right)^2 - 1\right]\frac{\sigma_{33}}{Z_{\mathrm{C}}} + \frac{\tau_{31}^2}{S_{31}^2} = 1
\end{aligned} \tag{12}$$

where $f_{1\mathrm{fT}}$ and $f_{1\mathrm{fC}}$ represent tension and compression fibre failure in the fibre direction; $f_{2\mathrm{mT}}$ and $f_{2\mathrm{mC}}$ denote in-plane transverse matrix cracking and matrix shear failure; $f_{3\mathrm{mT}}$ and $f_{3\mathrm{mC}}$ refer to out-of-plane transverse matrix cracking and matrix shear failure; X_{T} and X_{C} are the tensile and compressive strengths in the fibre direction; Y_{T} and Y_{C} are the in-plane transverse tensile and compressive strengths; Z_{T} and Z_{C}: the out-of-plane transverse tensile and compressive strengths; S_{12}, S_{23} and S_{31} are the shear strengths in the corresponding planes; and $\langle\rangle$ stands for the Macaulay brackets.

2.1.3.2. Anisotropic damage evolution. Damage evolution of the yarn material was described based on the formulations proposed by Chen and Aliabadi [31]. Specifically, the damage variable corresponding to a damage mode was assumed to comply with a modified Weibull distribution and evolve with a criterion defined in Eq. (12) and can be written in the following compact form:

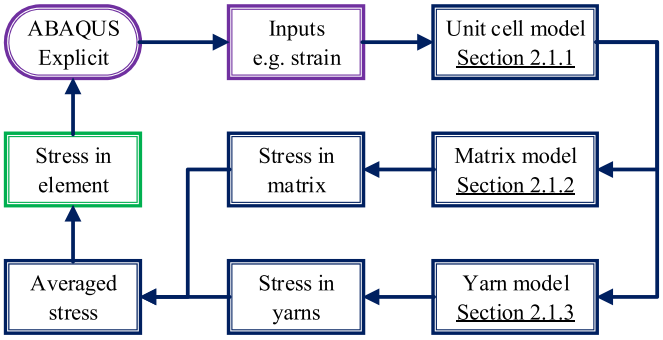

Fig. 5. Flowchart of the user-defined VUMAT subroutine.

$$\omega_{abC} = \begin{cases} 1 - \exp\left\{ -\frac{1}{e}\left[(f_{abC})^{\beta_{abC}} - 1 \right] \right\} & f_{abC} \geq 1 \\ 0 & f_{abC} < 1 \end{cases} \tag{13}$$

where f_{abC} (abC = 1fT, 1fC, 2mC, 2mS, 3mC, 3mS) is a damage criterion function; ω_{abC} stands for the corresponding damage evolution function; and β_{abC} is a material parameter reflecting the rate of damage evolution. It should be noted that more than one damage mode may occur if the yarn material is under multiaxial loading conditions, resulting in combined damage in the normal and shear directions. For this reason, the damage in the yarn material in different directions is defined as follows, where subscripts 1, 2 and 3 refer to the normal directions; and subscripts 4, 5 and 6 denote the shear directions:

$$\begin{aligned} \omega_1 &= \left(\omega_{1fT}\langle\sigma_{11}\rangle - \omega_{1fC}\langle-\sigma_{11}\rangle\right)/\sigma_{11} \quad \sigma_{11} \neq 0 \\ \omega_2 &= \left(\omega_{2mT}\langle\sigma_{22}\rangle - \omega_{2mC}\langle-\sigma_{22}\rangle\right)/\sigma_{22} \quad \sigma_{22} \neq 0 \\ \omega_3 &= \left(\omega_{3mT}\langle\sigma_{33}\rangle - \omega_{3mC}\langle-\sigma_{33}\rangle\right)/\sigma_{33} \quad \sigma_{33} \neq 0 \\ \omega_4 &= 1 - \left(1-\omega_{1fT}\right)\left(1-\omega_{1fC}\right)\left(1-\omega_{2mT}\right)\left(1-\omega_{2mC}\right) \\ \omega_5 &= 1 - \left(1-\omega_{2mT}\right)\left(1-\omega_{2mC}\right)\left(1-\omega_{3mT}\right)\left(1-\omega_{3mC}\right) \\ \omega_6 &= 1 - \left(1-\omega_{3mT}\right)\left(1-\omega_{3mC}\right)\left(1-\omega_{1fT}\right)\left(1-\omega_{1fC}\right) \end{aligned} \tag{14}$$

As a result of material damage, the linear constitutive relationship between the stress and strain does not hold and thus must be modified by including the damage variables defined in Eq. (14). In this work, the contributions of the damage variables to degradation in the yarn material ($\mathbf{C}^y$) were addressed by modifying the elasticity matrix, as follows:

$$\mathbf{C}^y = \left(\mathbf{S}^y(\boldsymbol{\omega})\right)^{-1} = \begin{bmatrix} \left(\mathbf{S}(\boldsymbol{\omega})_d\right) & 0 \\ 0 & \left(\mathbf{S}(\boldsymbol{\omega})_s\right) \end{bmatrix}^{-1} \tag{15}$$

$$\mathbf{S}(\boldsymbol{\omega})_d = \begin{bmatrix} \frac{1}{E_L(1-\omega_1)} & -\frac{\nu_{LT}}{E_L\sqrt{(1-\omega_1)(1-\omega_2)}} & -\frac{\nu_{TL}}{E_T\sqrt{(1-\omega_1)(1-\omega_3)}} \\ -\frac{\nu_{LT}}{E_L\sqrt{(1-\omega_1)(1-\omega_2)}} & \frac{1}{E_T(1-\omega_2)} & -\frac{\nu_{TT}}{E_T\sqrt{(1-\omega_2)(1-\omega_3)}} \\ -\frac{\nu_{TL}}{E_T\sqrt{(1-\omega_1)(1-\omega_3)}} & -\frac{\nu_{TT}}{E_T\sqrt{(1-\omega_2)(1-\omega_3)}} & \frac{1}{E_T(1-\omega_3)} \end{bmatrix} \tag{16}$$

$$\mathbf{S}(\boldsymbol{\omega})_s = \frac{1}{G_{LT}(1-\omega_4)} \quad \frac{1}{G_{TT}(1-\omega_5)} \quad \frac{1}{G_{TL}(1-\omega_6)} \tag{17}$$

where $\mathbf{S}^y(\boldsymbol{\omega})$ is the inverse of the damage elasticity matrix; $\mathbf{S}(\boldsymbol{\omega})_d$ and $\mathbf{S}(\boldsymbol{\omega})_s$ are the direct and shear components of the inverse matrix; E_L, E_T, G_{LT}, G_{TT} and G_{TL} are the elastic and shear moduli; and ν_{LT}, ν_{TT} and ν_{TL} are Poisson's ratios in the corresponding directions.

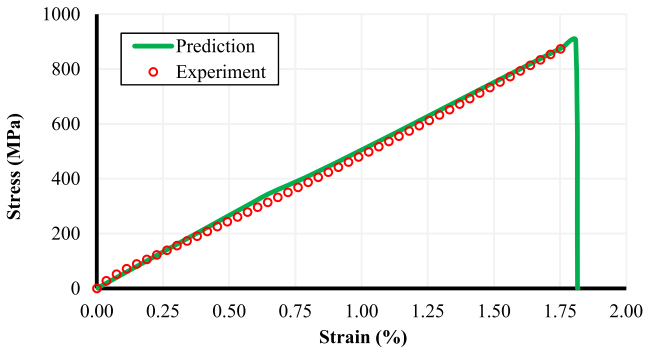

Fig. 6. Comparison of the predicted and measured stress-strain curves.

2.2. Modelling at mesoscale II

The modelling approach at mesoscale II addresses interlaminar delamination, which is one of the predominant failure modes in plain woven composites, due to the lack of binding yarns in the through-thickness direction. This research took the advantage of ABAQUS [32] by defining surface-based cohesive interaction to model interlaminar delamination. For completeness, a brief introduction to the theories employed in this work to describe interlaminar delamination is given in Appendix A.

2.3. Modelling at the macroscale

The modelling of plain woven composites at the macroscale was performed based on the commercial finite element (FE) code ABAQUS. It involves: 1) building the geometry of the composite structure under investigation; 2) developing a user-defined material subroutine to correlate the macroscopic behaviour of the composite with the micro-mechanical models described in Section 2.2; 3) assigning the user-defined material to the composite; 4) defining the required loading and boundary conditions; and 5) defining the contact conditions and cohesive interactions between adjacent plies. Further details regarding modelling at this scale will be presented in Section 3.

Here, it should be noted that the mesoscale models (i.e. the UC model and the constitutive models of the polymer matrix and yarn material) were implemented by developing a user-defined subroutine VUMAT within the framework of ABAQUS/Explicit. Fig. 5 shows the flowchart of this subroutine, which is called for all elements at every increment of the simulation. The subroutine starts by reading the inputs, e.g. the material parameters, the stress, strain and other variables at the previous step, and the strain increment at the current step. Based on the inputs, a uniform strain boundary condition is applied to the UC to calculate the

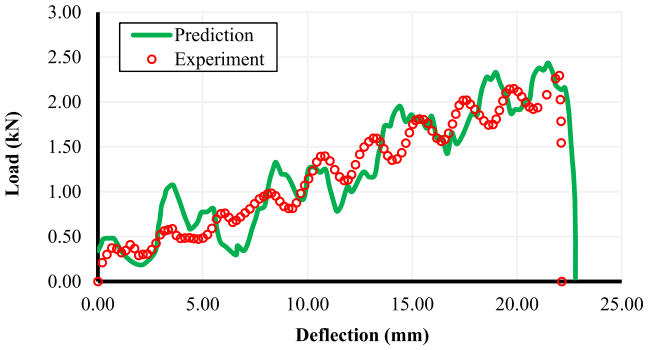

Fig. 7. Comparison of the predicted and measured load-deflection curves.

Table 1
Summary of the input & response parameters and their dependencies on the scaling factor.

Parameter		Name	Dimension	Scale factor
Input parameter	l	Specimen length	L	n
	w	Specimen width	L	n
	h	Specimen thickness	L	n
	d_i	Impactor diameter	L	n
	d_s	Support diameter	L	n
	E	Specimen modulus	$MT^{-2}L^{-1}$	1
	ρ	Specimen density	ML^{-3}	1
	ν	Specimen Poisson's ratio	–	1
	E_i	Impactor modulus	$MT^{-2}L^{-1}$	1
	ρ_i	Impactor density	ML^{-3}	1
	ν_i	Impact Poisson's ratio	–	1
	m_i	Impact mass	M	n^3
	V_i	Impact velocity	LT^{-1}	1
Response parameter	F_i	Contact force	$MT^{-2}L$	n^2
	t	Impact duration	T	n
	δ	Deflection	L	n
	E_I	Impact energy	$MT^{-2}L^2$	n^3

microscopic stresses in both the polymer matrix and the yarn material based on the constitutive models described in Sections 2.1.2 and 2.1.3. Finally, the macroscopic stress of an element or integration point is computed using the volume fractions and transformed microscopic stresses of different phases of material, as follows:

$$\langle\boldsymbol{\sigma}\rangle = \boldsymbol{\sigma}_{\mathrm{m}}\nu_{\mathrm{m}} + \sum_{1}^{n}\boldsymbol{\sigma}_{\mathrm{warp}}^{tii}\nu_{\mathrm{warp}}^{i} + \sum_{1}^{n}\boldsymbol{\sigma}_{\mathrm{fill}}^{tii}\nu_{\mathrm{fill}}^{i} \tag{18}$$

where $\langle\boldsymbol{\sigma}\rangle$ represents the homogenised or macroscopic stress; $\boldsymbol{\sigma}_{\mathrm{m}}$, $\boldsymbol{\sigma}_{\mathrm{warp}}^{tii}$ and $\boldsymbol{\sigma}_{\mathrm{fill}}^{tii}$ are the stresses in the matrix phase, the ith segment of the warp yarn and the ith segment of the fill yarn in the GCS of the UC; ν_{m}, ν_{warp}^{i} and ν_{fill}^{i} refer to the corresponding volume fractions.

2.4. Validation of the multiscale model in simple loading conditions

To validate the multiscale model, two numerical examples were conducted to analyse a plain woven carbon fibre-reinforced polymer composite (which will be described in Section 3.1) under two simple loading cases. The first example was to simulate a uniaxial tension test on a rectangular specimen loaded in the fibre direction at an overall strain-rate of 1×10^{-3} s^{-1}. Fig. 6 shows a comparison of the predicted and experimental stress-strain curves. Here, it is evident that the linear elastic behaviour of this plain woven composite subjected to tension in the fibre direction has been well predicted. Also, the predicted ultimate failure stress and strain (approximately 900 MPa @ 1.8%) agree well with those measured by the experimental test. The second example was to simulate a three-point bending impact on a rectangular beam with dimensions of 65 mm × 10 mm × 1.12 mm by a cylindrical impactor with an initial impact velocity of 3.13 m/s. Fig. 7 compares the simulated and measured load-deflection curves. The results suggest that the response of the composite under flexural impact loading has been reasonably predicted.

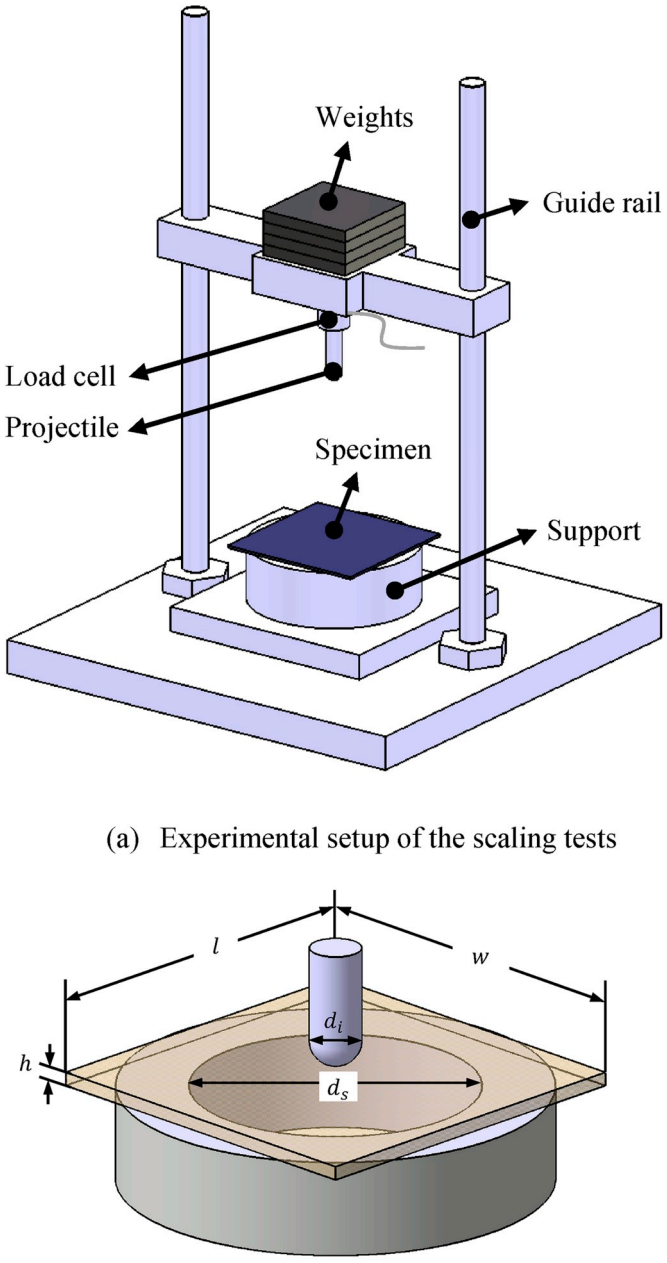

Fig. 8. Schematic of the scaling tests on the plain woven CFRP composite panels.

Table 2
Details of the four scaled impact tests.

Scale	Projectile diameter (mm)	Support inner diameter (mm)	Release height (mm)	Impact mass (kg)
n	d_i	d_s	H	m_i
1/4	5	50	500	0.54
1/2	10	100	500	4.36
3/4	15	150	500	14.70
1	20	200	500	34.84

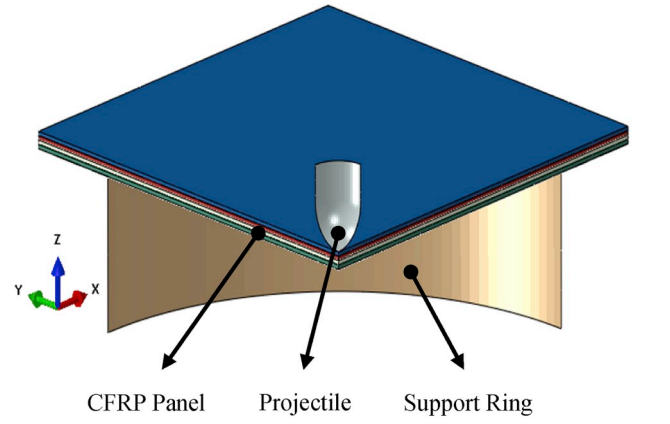

(a) Overview of the FE model

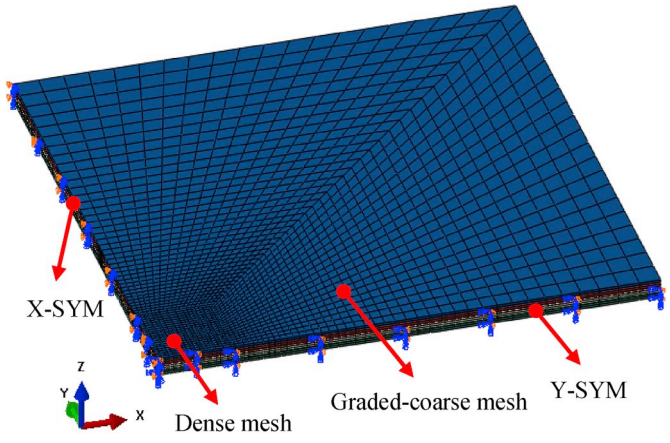

(b) Graded design of the mesh of the composite panel

Fig. 9. A typical scaled FE model of the low-velocity impact tests.

3. Results and discussion

3.1. Similitude approach

A prerequisite for a set of scaled test models to be valid for revealing any scaling effects is that these scaled models must be equivalent or similar [33], which can be ensured by applying the Buckingham π-theorem [34]. In this work, scaling effects in the low-velocity impact response of plain woven composites were investigated based on four similarly scaled models, and the approach adopted to ensure model similarity involves defining a number of independent π-terms based on a set of input and response parameters, whose dimensions are given in terms of the M-L-T fundamental types of dimensions, i.e. Mass (M), Length (L) and Time (T). As shown in Table 1, the input parameters include both geometrical and material parameters, while the response (or output) parameters are comprised of contact force, impact duration,

Table 3
Material properties of the composite under investigation.

Matrix	E_m (GPa)	ν_m	ε_{m0}	C_{me}	β_m		
	3.11	0.36	7.13%	0.014	3.8		
	D_0 (s^{-1})	n_r	Z_1 (MPa)	Z_0 (MPa)	q	α_1	α_0
	1×10^4	3.01	211.57	62.27	Eq. (19)	1.23	0.28
Yarn	E_L (GPa)	E_T (GPa)	ν_{LT}	ν_{TT}	G_{LT} (GPa)		
	161 64	10.57	0.27	0.33	5.52		
	X_T/X_C (MPa)	Y_T/Y_C (MPa)	Z_T/Z_C (MPa)	S_{12} (MPa)	S_{23} (MPa)	S_{31} (MPa)	
	2687/ 1622	58/ 263	58/263	95	78	80	
	β_1	β_2	β_3	β_4	β_5	β_6	
	9.0	7.6	4.7	2.8	4.7	2.8	
Interface	N (MPa)	S MPa)	T (MPa)	(J/ m^2)	G_{IIC} (J/m^2)	G_{IIIC} (J/m^2)	
	72.23	69.33	69.33	1300	4561	4561	

deflection and impact energy. By enforcing similarity requirements between the scaled models, explicit representation of the input and response parameters can be formulated in terms of an expression of the scaling factor (n), which is defined as the ratio of the characteristic length of the small-scale model to that of the full-scale model. It should be noted that the scaling laws given in the last column of Table 1 can be used to determine whether two scaled models are similar or equivalent. Specifically, if scaled models are built with their input parameters following the simple scaling laws defined in Table 1, these scaled models are called "similar" or "scalable" if the following conditions are met:

1) Contact force scales as the square of the scaling factor, i.e. n^2;
2) Impact time and deflection scale as the scaling factor, i.e. n;
3) Impact energy scales as the cube of the scaling factor, i.e. n^3.

3.2. Details of the scaling study

To utilise the multiscale model described in Section 2 to numerically investigate scaling effects in plain woven composites, four scaled FE models were created to simulate plain woven carbon fibre-reinforced polymer (CFRP) composite panels subjected to low-velocity impact on an instrumented drop-weight setup, as illustrated in Fig. 8. In each scaled test, a scaled square panel was freely placed onto a support ring and impacted at the centre by a hemispherical steel projectile released from a fixed height of 500 mm, yielding a constant initial impact velocity of 3.13 m/s. The projectile shed blocks were added to producing an impact energy of $170.7n^3$ J - The detailed dimensions and impact conditions of the scaled tests were determined according to the scaling

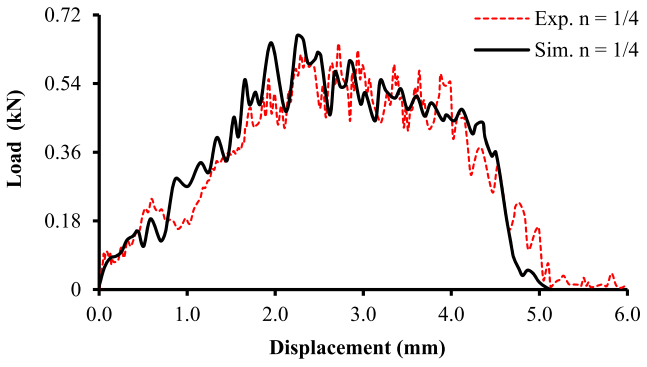

Fig. 10. Predicted and measured load-displacement curves of the n = 1/4 case.

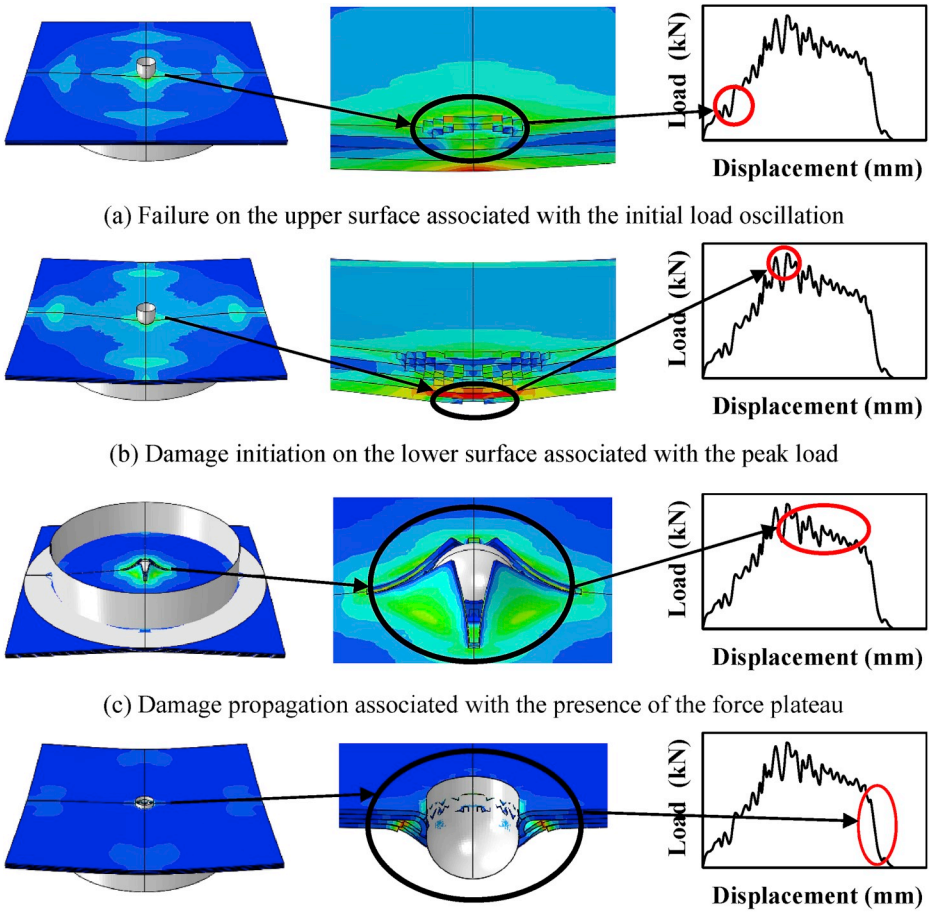

Fig. 11. Correlation between the load-displacement response and the impact damage.

laws listed in Table 1, and the corresponding values are summarised in Table 2.

Fig. 9 shows a scaled FE model for simulating the corresponding experimental test. Here, both the projectile and support ring were modelled using rigid shell elements, while the composite panel was treated as a deformable plate with a graded mesh design. To save computational costs, only a quarter of the actual geometry was created, and the falling motion of the projectile was replaced by assigning an initial velocity of 3.13 m/s, along with an appropriate inertia value.

The composite panels were manufactured from EP121-C15-53 prepreg provided by Gurit [30]. It consists of a 3k HTA carbon fibre plain woven fabric pre-impregnated with EP121 epoxy. The fabric has an areal density of 193 g/m^2. The resin is a highly-toughened system and has a weight fraction of 53%. In the as-supplied form, the prepreg has a nominal thickness of 0.28 mm and a fibre volume fraction of 39%. The material properties of the matrix and the yarn material and the interface parameters for interlaminar delamination are summarised in Table 3. Here, the first row of the matrix's properties was taken from Ref. [31], where the uniaxial tensile tests were performed on EP 121 to determine the elastic and ultimate failure strain properties. In terms of the parameters of the viscoplasticity model, they were determined after analysing the uniaxial tension test results obtained by Chen and Aliabadi [31], together with the properties of the yarn and the damage parameters, and shear tests on six samples were conducted at strain-rates of 1×10^{-5}, 1×10^{-4}, 1×10^{-3}, 1×10^{-2}, 1×10^{-1} and $1\ s^{-1}$, following the least-squares regression procedure. It should be noted that the value of parameter q is not fixed, but related to the effective strain-rate, as shown in Eq. (19). In terms of the parameters for interlaminar delamination,

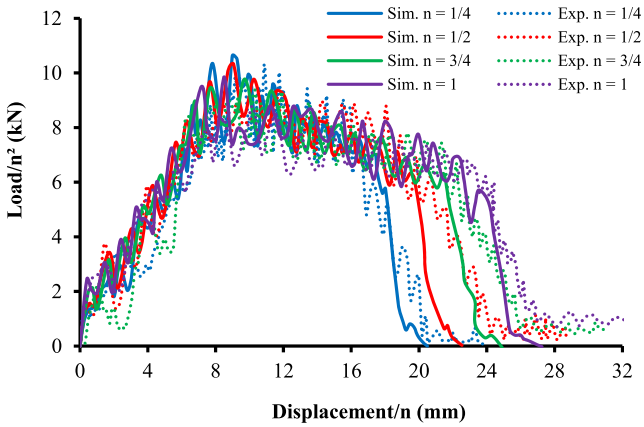

Fig. 12. Normalised load-displacement results following experimental scaling tests and FE simulations.

the interfacial strength properties (N, S, T) were determined from uniaxial tension tests on the EP 121 resin, while the fracture toughness properties (G_{IC}, G_{IIC}, G_{IIIC}) were approximated based on the EP121 based woven composite investigated by Yahya et al. [35].

$$q = \begin{cases} 0.53\ln(|\dot{\varepsilon}_{eff}|) + 69.65 & |\dot{\varepsilon}_{eff}| > \dot{\varepsilon}_0 \\ 0.53\ln(|\dot{\varepsilon}_0|) + 69.65 & |\dot{\varepsilon}_{eff}| \le \dot{\varepsilon}_0 \end{cases} \tag{19}$$

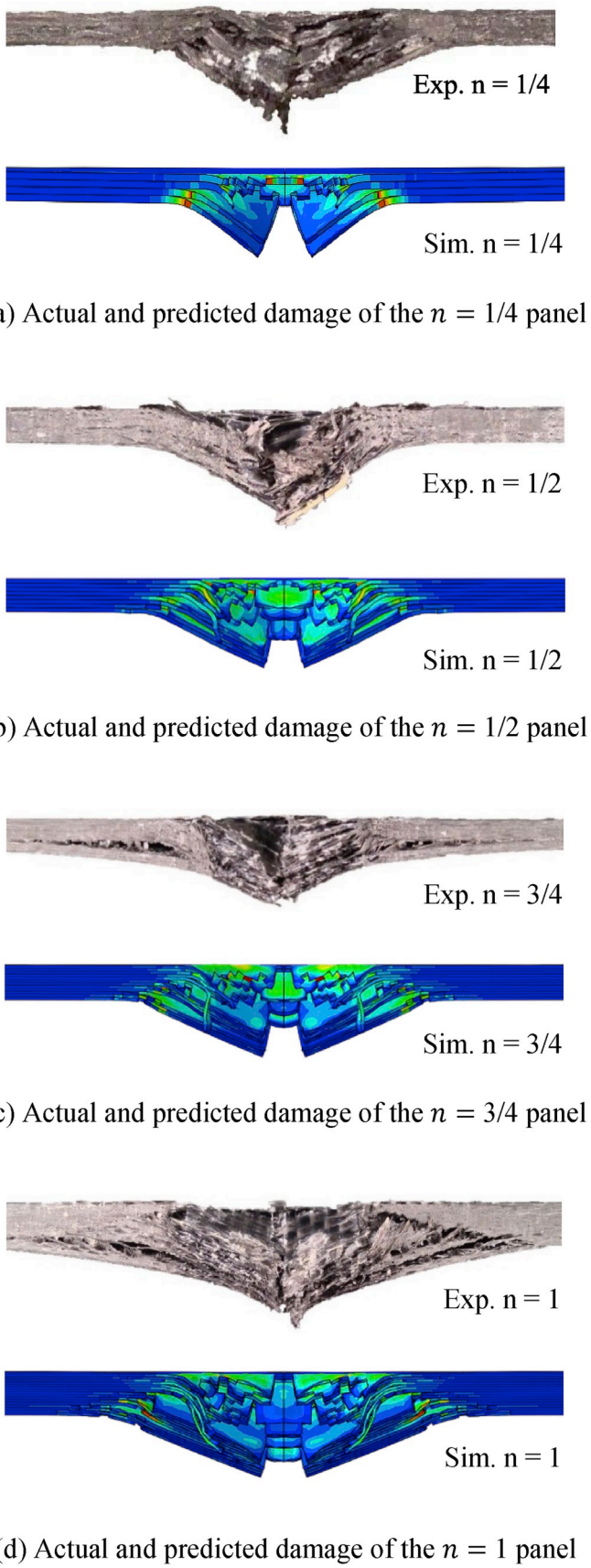

Fig. 13. The actual and predicted damage features on the middle cross-sections of the four scale sizes.

3.3. Scaling effects in the impact response

The load-displacement curve predicted following a simulation of the smallest (1/4) scale sample is shown in Fig. 10, where the experimental trace is also included. It is evident that the load-displacement curve predicted using the proposed multiscale model agrees well with that obtained by the test, with all major features of the load-displacement curve (such as the quasi-linear increase of the load with the displacement at the initial stage, the subsequent force plateau, and finally the rapid reduction in force) being successfully captured. In addition to obtaining the load-displacement result, damage in the composite panel at several time intervals was captured and is shown in Fig. 11, where the correlation between the load-displacement curve and the damage mechanism is highlighted. It can be seen by comparing Fig. 11(a) with Fig. 11(b) that failure on the upper surface, mainly due to indentation effects, resulted in some oscillations in the load during the initial quasi-linear stage, occurred earlier than the fibre failure on the lower surface. It can also be observed in Fig. 11(b) that the presence of the peak load coincides with the initiation of fibre fracture on the lower surface. Further, Fig. 11(c) suggests that the dominant damage mechanism was fibre fracture, extending away from the centre of the panel in both the warp and fill directions, producing an almost constant force in the load-displacement curve. Finally, the load rapidly dropped to zero due to target perforation, as shown in Fig. 11(d).

The predicted load-displacement curves for the other three scales also agree reasonably well with the experimental curves. However, due to space restrictions, only the normalised results (the load data and the displacement data were divided by n^2 and n, according to the scaling laws given in Table 1) are shown in Fig. 12 for analysing scaling effects in the load-displacement response. As displayed in this figure, all of the predicted curves exhibit similar trends to their corresponding experimental traces, indicating that scaling effects in the load-displacement at different impact stages have been well captured using the multiscale model. For instance, during the initial quasi-linear stage, the predicted curves collapse in the same way as do the experimental counterparts onto a single curve, suggesting that the load-displacement response during this stage obeys a simple scaling law. Similarly, the trend in the force plateaus where the experimental curves become increasingly lengthened with scale size was predicted by the FE simulations. Here, it should be noted that the increase in the length of the force plateau indicates a prolonged period of damage propagation in the larger scales. Given that the load and displacement data were normalised according to the scaling laws listed in Table 1, the variation of the force plateau (which is associated with crack propagation in the panel) indicates that impact damage in this composite does not obey a simple scaling law, but becomes more severe as the scale size increases.

The accuracy of the proposed multiscale model was further evaluated by comparing the predicted damage features against those observed in the scaling tests. As clearly shown in Fig. 13, both the primary failure modes (i.e. fibre fracture along the centre lines of the panel and some degree of interlaminar delamination) and the appearance of the

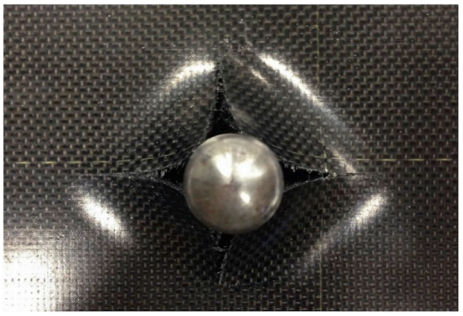

Fig. 14. Rear view of a perforated panel showing a wide crack opening.

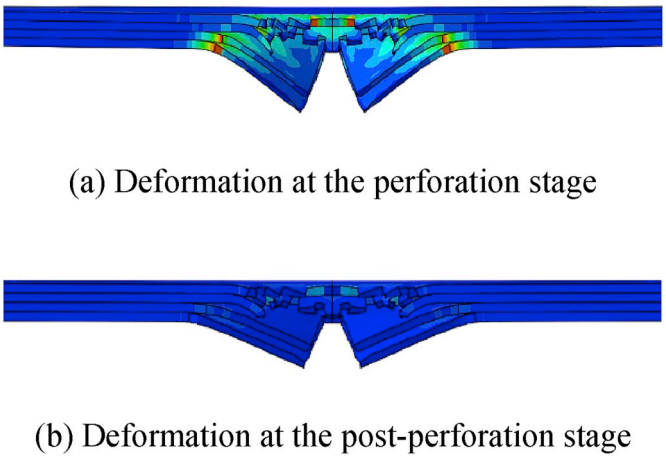

Fig. 15. Simulated spring-back of the smallest panel after projectile perforation.

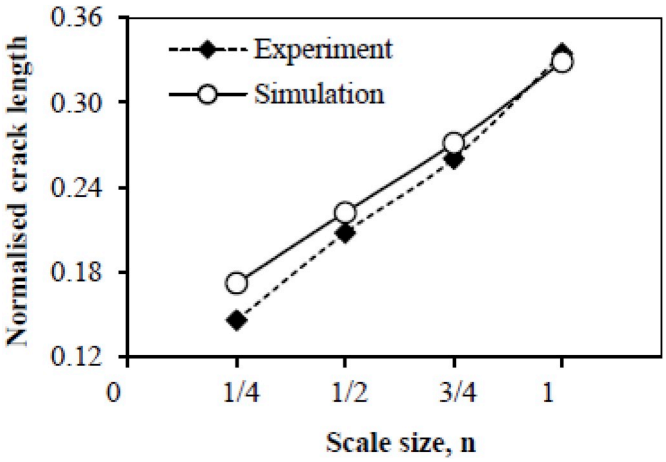

Fig. 16. The predicted and measured normalised crack lengths for the four scale sizes.

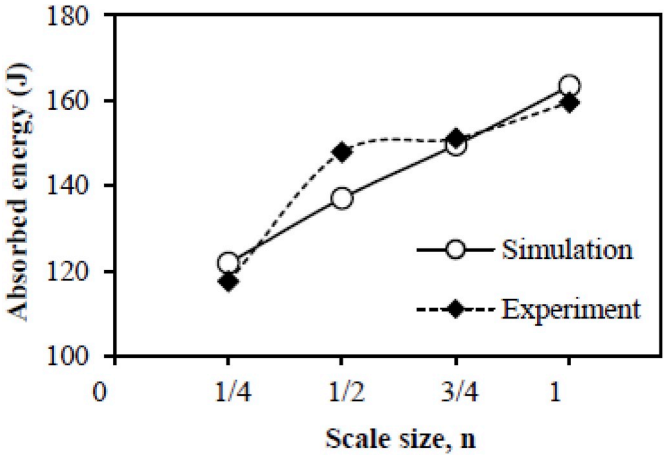

Fig. 17. The predicted and measured normalised energies for the four scale sizes.

damaged area in each scale size have been reasonably simulated. It should be noted that all the simulated panels appear to exhibit a wider crack opening than their experimental counterparts, which is attributed to the reasons below. Firstly, the formation of cracks in these FE models was simulated by deleting failed elements, whereas no material was removed in the sample tested. Also, the cross-sectional views of the four scaled panels were taken after the projectiles being manually removed. As the removal of the projectiles caused spring-back of the material near the cracks, it resulted in almost closed crack openings, in comparison to the state where the projectiles remained in place, as exemplified in Fig. 14. Further, the FE simulations were terminated shortly after the projectiles fully perforated the panels to save computational time. As a result, spring-back of the undamaged material near the cracks was not simulated, leading to wider openings in the simulated cracks. However, an additional FE simulation was performed for the case of the smallest scale size. By comparing the deformation of the panel at the perforation stage with that at a post-perforation stage, as shown in Fig. 15, the capability of the proposed model in simulating spring-back can be qualitatively confirmed.

The capability of the proposed multiscale model to predict scaling effects in the impact response was further scrutinised by analysing the normalised crack length on the back face of the panel and the normalised absorbed energy, as shown in Figs. 16 and 17, respectively. From Fig. 16, it is evident that the data points associated with the variation of the predicted crack length with scale size coincide with the experimental data, with both curves suggesting a roughly linear increase in the normalised crack length with scale size. Again, the experimental evidence indicates that damage in the test panels does not obey a scaling law, and the numerical data support this conclusion. In terms of the normalised energy absorption, the predicted results generally agree well with the experimental data, except for the case of the second scale size where there is some discrepancy between the experimental and the predicted values, i.e. 147.9 vs 137.0 J (Fig. 17). However, it is believed that there should be a linear trend in the normalised energy, despite the scattered experimental data of the second scale size, as both the experimental data for the other three cases and the numerical results confirm this. In general, the results shown in Figs. 16 and 17 once again confirm the capability of the multiscale model in predicting scaling effects in the impact response of these plain woven composite panels.

4. Conclusions

A multiscale model has been developed to numerically investigate scaling effects in the impact response of plain woven composites. The model features developing a parameterised UC to account for the internal architecture and employing existing material models to describe the microscopic behaviour of the constituents, including the rate-dependent nonlinearity of the matrix and the anisotropic damage of the yarn material. The proposed model was implemented by developing a user subroutine and validated by two simple loading cases and four numerical examples performed to simulate a set of scaled plain woven composite panels subjected to scaled projectile impact. Scaling effects predicted were compared with those observed in the experiments, highlighting reasonable predictions of both scalable and non-scalable scaling effects. Specifically, it was shown that the load-displacement response of the composite is scalable at the initial elastic stage and becomes non-scalable since the normalised curves become increasingly extended due to the presence of lengthened force plateaus. In addition, although there was no transition in the primary failure mode, significant non-scalable scaling effects in impact damage were predicted, with the normalised size of damage increasing with scale size. Further, non-scalable scaling effects in the absorbed energy were predicted, which again suggests that damage in this composite does not obey a simple scaling law, with impact damage becoming more severe with increasing scale size.

Declaration of competing interest

The authors declare that they have no known competing financial interests or personal relationships that could have appeared to influence

the work reported in this paper.

CRediT authorship contribution statement

Z.W. Xu: Writing - original draft, Methodology, Software. **Y.H. Chen:** Methodology. **W.J. Cantwell:** Supervision, Writing - review & editing. **Z.W. Guan:** Supervision, Writing - review & editing.

Acknowledgements

The lead author Z. W. Xu gratefully acknowledges the financial support from the China Scholarship Council (CSC) under Grant number 201408060025.

Appendix A. Cohesive interface modelling

In this work, the interfaces between the composite plies were described using the bilinear traction-separation model in ABAQUS. It assumes that the response of a cohesive interface is linear elastic prior to the onset of delamination, followed by a linear damage degradation on the propagation of delamination. In the initial elastic region, the constitutive behaviour is defined in terms of an elasticity matrix relating the traction to the separation, as follows:

$$\boldsymbol{t} = \begin{Bmatrix} t_{\mathrm{n}} \\ t_{\mathrm{s}} \\ t_{\mathrm{t}} \end{Bmatrix} = \begin{bmatrix} K_{\mathrm{nn}} & K_{\mathrm{ns}} & K_{\mathrm{nt}} \\ K_{\mathrm{ns}} & K_{\mathrm{ss}} & K_{\mathrm{st}} \\ K_{\mathrm{nt}} & K_{\mathrm{st}} & K_{\mathrm{tt}} \end{bmatrix} \begin{Bmatrix} \delta_{\mathrm{n}} \\ \delta_{\mathrm{s}} \\ \delta_{\mathrm{t}} \end{Bmatrix} = \mathbf{K}\boldsymbol{\delta} \tag{A.1}$$

where t_{n}, t_{s} and t_{t} are the normal and two shear stress components of the traction vector $\boldsymbol{t}$; δ_{n}, δ_{s} and δ_{t} represent the relative displacements between the connected surfaces in the normal and shear directions; and $\mathbf{K}$ stands for the elasticity matrix. In terms of the onset of delamination, it was determined using a quadratic criterion proposed by Ye [36]:

$$f_{\mathrm{d}} = \left(\frac{\langle t_{\mathrm{n}} \rangle}{N}\right)^2 + \left(\frac{t_{\mathrm{s}}}{S}\right)^2 + \left(\frac{t_{\mathrm{t}}}{T}\right)^2 = 1 \tag{A.2}$$

where N, S and T represent the normal and two shear strengths of the interface; the Macaulay brackets $\langle\rangle$ ensure that only the tensile normal traction is used in identifying the onset of delamination.

In terms of the propagation of delamination, a scalar damage variable, D, was defined to account for the linear degradation of the elasticity matrix due to mixed-mode delamination:

$$\mathbf{K}_{\mathrm{d}} = D\mathbf{K} \quad D = \frac{\delta_{\mathrm{m}}^{\mathrm{f}}\left(\delta_{\mathrm{m}}^{\max} - \delta_{\mathrm{m}}^{\mathrm{o}}\right)}{\delta_{\mathrm{m}}^{\max}\left(\delta_{\mathrm{m}}^{\mathrm{f}} - \delta_{\mathrm{m}}^{\mathrm{o}}\right)} \tag{A.3}$$

where $\mathbf{K}_{\mathrm{d}}$ refers to the damaged elasticity matrix; D is the damage variable; $\delta_{\mathrm{m}}^{\max}$ stands for the maximum value of the effective separations attained in the whole loading history; and $\delta_{\mathrm{m}}^{\mathrm{o}}$ and $\delta_{\mathrm{m}}^{\mathrm{f}}$ are the separations corresponding to the onset of delamination and failure. Here, it must be noted that the values of $\delta_{\mathrm{m}}^{\mathrm{o}}$ and $\delta_{\mathrm{m}}^{\mathrm{f}}$ vary with the mixed-mode ratio. The former was determined as a function of the strength values and the mixed-mode ratio [37], while the latter was treated using the BK criterion [38] and associated with the fracture toughness properties, i.e. Mode I (opening) fracture toughness, G_{IC}, Mode II (sliding) fracture toughness, G_{IIC}, and Mode III (tearing) fracture toughness, G_{IIIC}.

Appendix B. Supplementary data

Supplementary data to this article can be found online at https://doi.org/10.1016/j.compositesb.2020.107885.

References

[1] Wisnom MR. The effect of specimen size on the bending strength of unidirectional carbon fibre-epoxy. Compos Struct 1991;18:47–63.
[2] Jackson KE, Kellas S, Morton J. Scale effects in the response and failure of fiber reinforced composite laminates loaded in tension and in flexure. J Compos Mater 1992;26(18):2674–705.
[3] Kellas S, Morton J. Strength scaling in fiber composites. AIAA J 1992;30(4):1074–80.
[4] Sutherland LS, Shenoi RA, Lewis SM. Size and scale effects in composites: II. Unidirectional laminates. Compos Sci Technol 1999;59(2):221–33.
[5] Green BG, Wisnom MR, Hallett SR. An experimental investigation into the tensile strength scaling of notched composites. Compos Appl Sci Manuf 2007;38(3):867–78.
[6] Wisnom MR, Hallett SR, Soutis C. Scaling effects in notched composites. J Compos Mater 2009;44(2):195–210.
[7] Mohammed Y, Hassan MK, El-Ainin HA, Hashem AM. Size effect analysis of open-hole glass fiber composite laminate using two-parameter cohesive laws. Acta Mech 2014;226(4):1027–44.
[8] Morton J. Scaling of impact-loaded carbon-fiber composites. AIAA J 1988;26(8):989–94.
[9] Cantwell WJ, Morton J. Geometrical effects in the low velocity impact response of CFRP. Compos Struct 1989;12:35–59.
[10] Swanson SR. Scaling of impact damage in fiber composites from laboratory specimens to structures. Compos Struct 1993;25(1):249–55.
[11] Carrillo JG, Cantwell WJ. Scaling effects in the low velocity impact response of fiber-metal laminates. J Reinforc Plast Compos 2008;27(9):893–907.
[12] McKown S, Cantwell WJ, Jones N. Investigation of scaling effects in fiber-metal laminates. J Compos Mater 2008;42(9):865–88.
[13] Yang FJ, Hassan MZ, Cantwell WJ, Jones N. Scaling effects in the low velocity impact response of sandwich structures. Compos Struct 2013;99:97–104.
[14] Ishikawa T, Chou TW. Elastic behavior of woven hybrid composites. J Compos Mater 1982;15(1):2–19.
[15] Wentorf R, Collar R, Shephard MS, Fish J. Automated modeling for complex woven mesostructures. Comput Methods Appl Mech Eng 1999;172(1–4):724–47.
[16] Lomov SV, Gusakov AV, Huysmans G, Prodromou A, Verpoest I. Textile geometry preprocessor for meso-mechanical models of woven composites. Compos Sci Technol 2000;60(11):2083–95.
[17] Whitcomb J, Tang XD. Effective moduli of woven composites. J Compos Mater 2001;35(23):2127–44.
[18] Sun BZ, Liu YK, Gu BH. A unit cell approach of finite element calculation of ballistic impact damage of 3-D orthogonal woven composite. Compos B Eng 2009;40(6):552–60.
[19] Li LY, Aliabadi MH, Wen PH. Meshfree modelling and homogenisation of 3D orthogonal woven composites. Compos Sci Technol 2011;75(11):1777–88.
[20] Lin H, Zeng XS, Sherburn M, Long AC, Clifford MJ. Automated geometric modelling of textile structures. Textil Res J 2012;82(16):1689–702.

[21] Green SD, Matveev MV, Long AC, Ivanov D, Hallett SR. Mechanical modelling of 3D woven composites considering realistic unit cell geometry. Compos Struct 2014; 118:284–93.
[22] Hashin Z. Failure criteria for unidirectional fiber composites. J Appl Mech 1980;47: 329–34.
[23] Puck A, Schurmann H. Failure analysis of FRP laminates by means of physically based phenomenological models. Compos Sci Technol 1998;58:1045–67.
[24] Pinho ST, Dávila CG, Camanho PP, Iannucci L, Robinson P. Failure models and criteria for FRP under in-plane or three-dimensional stress states including shear non-linearity. Hampton, VA: NASA; 2005.
[25] Kaddoura AS, Hinton MJ, Soden PD. A comparative study of failure theories and predictions for fibre polymer composite laminates: Part (A). Composites 2000: 644–701.
[26] Fish J, Shek K. Computational plasticity and viscoplasticity for composite materials and structures. Compos B Eng 1998;29(5):613–9.
[27] Goldberg RK, Roberts GD, Gilat A. Incorporation of mean stress effects into the micromechanical analysis of the high strain rate response of polymer matrix composites. Compos B Eng 2003;34:151–65.
[28] Weeks CA, Sun CT. Modelling non-linear rate-dependent behaviour in fibre-reinforced composites. Compos Sci Technol 1998;58:603–11.
[29] Li S, Zhou C, Yu H, Li L. Formulation of a unit cell of a reduced size for plain weave textile composites. Comput Mater Sci 2011;50(5):1770–80.
[30] Gurit. Datasheet/EP121 - epoxy prepreg co-curable with phenolics. Available: http://www.gurit.com/-/media/Gurit/Datasheets/ep-121pdf.ashx; 2018.
[31] Chen YH, Aliabadi MH. Micromechanical modelling of the overall response of plain woven polymer matrix composites. Int J Eng Sci 2019;145.
[32] Dassault Systems. Abaqus analysis user's guide (version: 6.14) [Online].
[33] Jackson KE. Scaling effects in the flexural response and failure of composite beams. AIAA J 1992;30(8):2099–105.
[34] Buckingham E. On physically similar systems; Illustrations of the use of dimensional equations. Phys Rev 1914;4(4):345–76.
[35] Yahya MY, Cantwell WJ, Langdon GS, Nurick GN. The blast resistance of a woven carbon fibre-reinforced epoxy composite. J Compos Mater 2011;45(7):789–801.
[36] Ye L. Role of matrix resin in delamination onset of growth in composite laminates. Compos Sci Technol 1988;33(4):257–77.
[37] Camanho PP, Dávila CG. Mixed-mode decohesion finite elements for the simulation of delamination in composite materials. Hampton, Virginia: NASA; 2002.
[38] Benzeggagh ML, Kenane M. Measurement of mixed-mode delamination fracture toughness of unidirectional glass/epoxy composites with mixed-mode bending apparatus. Compos Sci Technol 1996;56(4):439–49.